K-edge resonant x-ray magnetic scattering from $RbMnF_3$

A. Stunault*
European Synchrotron Radiation Facility, Boîte Postale 220, F-38043 Grenoble Cedex, France

F. de Bergevin
Laboratoire de Cristallographie, CNRS, 166X, F-38042 Grenoble Cedex, France

D. Wermeille† and C. Vettier
European Synchrotron Radiation Facility, Boîte Postale 220, F-38043 Grenoble Cedex, France

Th. Brückel
Institut für Festkörperforschung, Forschungszentrum Jülich, D-52425, Jülich, Germany

N. Bernhoeft‡
European Synchrotron Radiation Facility, Boîte Postale 220, F-38043 Grenoble Cedex, France

G. J. McIntyre
Institut Laue Langevin, Boîte Postale 156, F-38042 Grenoble Cedex 9, France

J. Y. Henry
Centre d'Etudes Nucléaires, DRFMC/SPSMS/MDN, F-38054 Grenoble Cedex 9, France

(Received 5 May 1999)

Magnetic resonant x-ray scattering experiments at the Mn *K* edge have revealed the occurrence of two different resonances in antiferromagnetic $RbMnF_3$. Below the *K* edge, at the $3d$ threshold, the resonance profile is consistent with quadrupole electrical transitions from the $1s$ core level to the $3d$ states; the observed resonance amplitude corresponds to the expected value for spin-orbit splitting in $3d$ levels. The resonance at the $4p$ threshold extends over the whole $4p$ band; it is explained on the basis of electric dipole transitions which involve both spin-orbit splitting and exchange splitting of the $4p$ states. [S0163-1829(99)11937-4]

I. INTRODUCTION

Resonant x-ray magnetic scattering (RXMS) has become a widely used technique for the study of magnetism. The resonant enhancements, the chemical and electronic selectivity of the magnetic x-ray scattering cross section, have allowed important breakthroughs in the study of magnetic systems. However, the full use of this method rests on the assumption that the resonant scattering amplitude is directly and simply related to the local magnetization. Although an example of RXMS was observed by Namikawa *et al.* at the *K* edge of nickel metal,[1] most of the experimental studies have dealt with $L_{2,3}$ and $M_{4,5}$ edges of lanthanide and actinide compounds. In the theoretical model based on electric multipole transitions presented by Hannon *et al.*[2] to account for the observation of RXMS in pure holmium,[3] the magnetic resonance finds its origin in the asymmetry of the transition probabilities arising from the spin polarization of the intermediate states coupled with spin-orbit splittings either in the core levels or in the excited states. For this reason, the proposed mechanism is likely to apply to the spin-orbit split $L_{2,3}$ and M_{2-5} edges. However, the resonance at the *K* edge would have to rely primarily upon spin-orbit effects in the excited levels. As a result, the dipole ($E1$) transitions to $4p$ states are expected to have a weak contribution because of the small spin-orbit coupling in the *p* states and their weak spin polarization. Furthermore, Lovesey *et al.* have shown that quadrupolar ($E2$) transitions to $3d$ levels at the *K* edge are induced by the orbital moment of the $3d$ states of the atomic ground state;[4,5] it was predicted[4] that in the absence of such an orbital moment, splittings in the $1s$ level could lead to weak $E2$ resonances without rotation of the polarization. Consequently, $E1$ and $E2$ magnetic resonances at *K* edges in $L=0$ ground-state systems should be less pronounced than resonances at spin-orbit split edges such as the $L_{2,3}$ and $M_{4,5}$ edges. In contrast with these ideas, Namikawa *et al.* had introduced a different model based on transition operators to $4p$ levels involving both the electron spin and the photon electrical field, in order to explain the magnetic resonance observed at the Ni *K* edge.[1] This model does not require spin-orbit coupling but does require a net spin polarization of the $4p$ states.

In general, it appears that the experimental results at the $L_{2,3}$ and $M_{4,5}$ edges can be interpreted from a simple atomic view of the resonant process within the scope of Hannon's model. However, recent experimental results have shown that the interpretation of RXMS and spin-polarized x-ray absorption data is more involved, even in the case of $4f$ and $5f$ systems. In particular, experiments at the L_2 and L_3 edges of Dy in $DyFe_4Al_8$ have indicated that it is necessary to go beyond simple atomic physics to account for the observed results.[6] It is worth noting that in all systems studied so far,

the resonances at the $L_{2,3}$ and $M_{4,5}$ edges have shown well-defined resonant energies; even when an energy splitting occurs, the energies involved are in the 0.5–2.0 eV range, and their physical origin can be found in exchange splitting. This is to be contrasted with the observations of the *K*-edge resonances in $3d$ systems[7–9] where magnetic resonances have been detected at the $E2$ and $E1$ threshold; the $E2$ peaks are sharp but the $E1$ resonance extends over an energy width of the order of 10 eV, comparable to the $4p$ band width. Furthermore, the resonance at the *K* edge can have a nonmagnetic character due to the sensitivity of the $4p$ states to the lattice symmetry.[10–12] Several studies of magnetic x-ray dichroism have revealed the existence of resonant effects at the *K* edge of $3d$ elements and compounds.[13–15] It is the purpose of this work to investigate the polarization and energy dependence of the x-ray magnetic cross section near the *K* edge of an $L=0$ system in order to discriminate between possible origins for the resonance, while avoiding complex lattice effects. For this purpose we have chosen to study Mn compounds where the Mn atoms are in the $3d^5$ configuration. Among the salts which can be formed with Mn^{2+} ions, some have a noncubic local symmetry, such as MnF_2, which leads to nonmagnetic resonant scattering[12] or exhibit large magnetostriction effects like MnO.[16] We have therefore selected the perovskite structure of $RbMnF_3$ which does not suffer from either of these effects.

$RbMnF_3$ has a simple-cubic structure (O_h^1 space group, $a=4.223$ Å at $T=20$ K) and orders antiferromagnetically below the Néel temperature $T_N=83.6$ K with a propagation vector $(\frac{1}{2},\frac{1}{2},\frac{1}{2})$. The magnetic moments lie along the $\langle 111\rangle$ direction and form alternating ferromagnetic $\{111\}$ planes.[17,18] There exist four magnetic domains corresponding to the four moment directions which all contribute to the scattering at any magnetic Bragg peak. A very small trigonal distortion of the cubic structure develops below T_N.[19] Nevertheless, because its magnetic anisotropy is negligible,[20] $RbMnF_3$ has been classified as the closest known physical realization of an isotropic three-dimensional (3D) Heisenberg antiferromagnet.[21] Indeed, the Mn^{2+} ions are in an $L=0$ ground state of the $3d^5$ configuration. The presence of a weak spin-orbit coupling in the $3d$ levels has been invoked to account for the observation of linear dichroism in the visible light range.[22] These characteristics make $RbMnF_3$ a suitable material to study possible origins of resonant enhancement of magnetic x-ray scattering.

We have organized the presentation of our work as follows: After the description of the experimental conditions in Sec. II, we report our experimental observations of the x-ray magnetic scattering near the manganese *K* edge in Sec. III. A discussion of the various models is given in Sec. IV, followed by the comparison with the experimental data in Sec. V. Finally, we present tentative perspectives for future work to elucidate the origin of resonant magnetic x-ray scattering at the *K* edge.

II. EXPERIMENTAL CONDITIONS

A preliminary x-ray study of the magnetic resonance at the Mn *K* edge in $RbMnF_3$ was performed at HASYLAB, at the wiggler beamline W1. Although resonant effects could be observed, the measured intensities were too weak to allow for complete polarization analysis in good conditions. Further difficulties arose since the energy resolution was not sufficient to separate the observed resonances. This paper describes the results of x-ray experiments conducted at the European Synchrotron Radiation Facility (ESRF) magnetic-scattering beamline ID20.

ID20 is the beamline at ESRF that is dedicated to magnetic scattering studies.[23] It receives x rays from a straight section which accommodates several insertion devices. During the experiments at ID20 described below, a 48-mm-period undulator was used. For the first experiment, only the second harmonic could be used to provide photons near the manganese *K* edge at 6.539 keV, whereas during the second experiment, thanks to a new vacuum chamber, the undulator gap could be closed further to reach the manganese *K*-edge energy with the third harmonic of the undulator. This constituted an important improvement in the experimental conditions for two reasons: (1) for a given energy bandwidth, the photon flux is higher at an odd harmonic; (2) the photon beam is better polarized at odd harmonics, and this effect is enhanced by the possibility of using a narrower radiation cone. The beamline optics consists of a double Si (111) crystal monochromator mounted between two vertically focusing Si mirrors. Sagittal focusing is achieved with the second monochromator Si crystal. The monochromaticity of the incident beam was measured to be 1.4×10^{-4} leading an energy resolution of 0.9 eV (full width at half maximum) at the Mn *K* edge. In the first experiment, the primary slits before the optics were opened to 1×1 mm^2, resulting in a photon flux at the sample of $\approx10^{12}$ photon/s/200 mA; they could be closed down to 0.5×0.5 mm^2 in the second experiment, with a slightly higher photon flux (2×10^{12} photons/s/200 mA), resulting in a spot size of the focused beam at the sample position of 0.6 (horizontal)$\times$0.3 (vertical) mm^2 in both cases. The measured degree of incident horizontal linear polarization was 85% and 96%, respectively. The linear polarization of the scattered beam was analyzed using the (030) Bragg reflection from a sapphire crystal Al_2O_3, with a Bragg angle of 43.6° at the Mn *K* edge. The measured peak reflectivity of the analyzer crystal was 11% at 6.5 keV. Corrections to account for the departure from the ideal 45° position[24] were neglected. The Al_2O_3 crystal has a mosaic spread of 0.022°. Such a narrow width makes it difficult to integrate correctly intensities at various *Q* positions and no effort was made to deconvolute the *Q*-resolution effects. Furthermore, a quantitative comparison of the intensities measured in the different polarization channels is difficult due to the complex change in the resolution function, even if rocking curves of the analyzer crystal were found to be almost identical in the two polarization channels $\sigma\rightarrow\sigma$ and $\sigma\rightarrow\pi$. On the other hand, the energy bandpass of this analyzer crystal is less than 3 eV, which allowed us to eliminate efficiently the fluorescence background, more than 40 eV below the edge. The *Q* dependence of integrated intensities could be measured more accurately without polarization analysis. Typical count rates were around 3500 counts/s at the $(\frac{1}{2},-\frac{1}{2},\frac{5}{2})$ reflection at the $E1$ resonance above a fluorescent background of 13 000 counts/s without the analyzer crystal. The Al_2O_3 crystal reduced the background to a few counts/s.

The $RbMnF_3$ sample used for these studies was a single crystal cut with its face perpendicular to the (001) direction

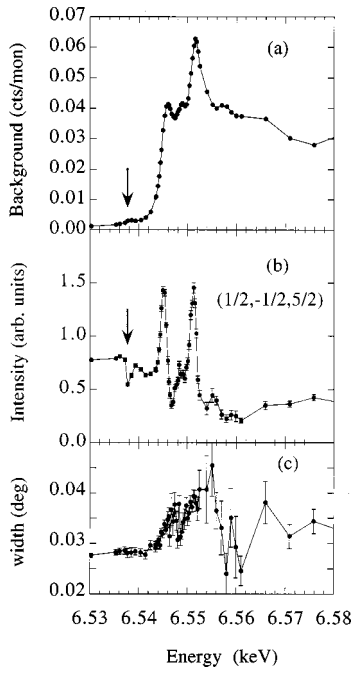

FIG. 1. Energy dependence of the integrated intensity (b), the fluorescence background (a) and the linewidth (c) of the rocking curves measured at the $(\frac{1}{2},-\frac{1}{2},\frac{5}{2})$ reflection. The data are not corrected for absorption. The arrows in (a) and (b) point to the quadrupolar features. The lines are guides to the eye.

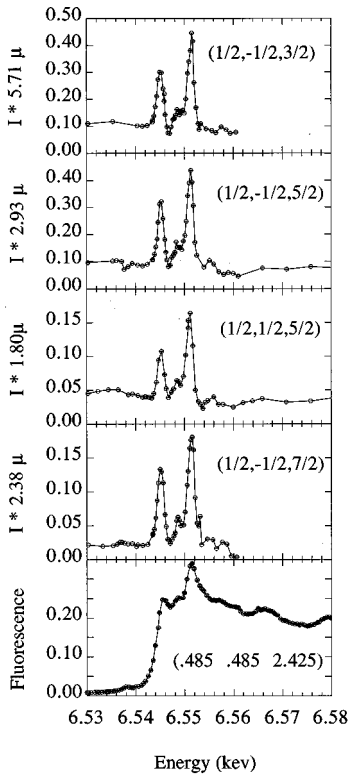

FIG. 2. Energy dependence of several magnetic reflections, corrected for absorption. The bottom panel shows the fluorescence measurement. The different coefficients in the *y*-axis legends come from the $\sin\alpha_0/\sin\alpha_1$ geometrical coefficient in the absorption. The lines are guides to the eye.

and mechanically polished. The measured mosaic spread of the (002) reflection at 6.50 keV—i.e., below the absorption edge—was 0.032(4)°. It actually increased to 0.041(5)° at 6.55 keV, close to the maximum of the absorption. A simple interpretation relates to a poorer crystal quality close to the surface, due to sample preparation (cutting and mechanical polishing): the penetration depth—which can be in first approximation taken as equal to $1/[\mu * \sin(\alpha_0)]$, α_0 being the incidence angle—decreases from 10 to 4 μm when varying the energy from 6.5 to 6.55 keV, which makes diffraction peaks more sensitive to the quality of the near-surface region.

The sample was mounted in a closed-cycle refrigerator on the ID20 diffractometer. The scattering plane was vertical with incident linear σ polarization. The orientation was chosen to have both (001) and (110) cubic axes in the scattering plane, when the surface normal was in the scattering plane. This gave access to the $(\frac{1}{2},\frac{1}{2},l+\frac{1}{2})$ magnetic Bragg peaks $(l=1,2,3)$ in a nonspecular scattering geometry, and to $(\frac{1}{2},-\frac{1}{2},l+\frac{1}{2})$ in an inclined geometry. Integrated intensities were deduced from the measured rocking curves of the sample, and normalized to a monitor intensity. Numerically, they were obtained by fitting a constant background and a $(\text{Lorentzian})^{3/2}$ to the data. This line shape was not chosen for any physical reasons, but only for the fact that it modeled best the observed rocking curves. The footprint-absorption corrections were performed on the integrated intensities, using $I_{\text{corr}}=I_{\text{meas}}*\mu*(1+\sin\alpha_0/\sin\alpha_1)$ where α_0 and α_1 are the angles of the incoming and outgoing beams with the sample surface. The energy-dependent absorption coefficient μ has been deduced from transmission measurements through a $RbMnF_3$ powder sample.

III. RESONANT SCATTERING RESULTS

Magnetic Bragg peaks were observed at $(h/2,k/2,l/2)$ positions in the reciprocal lattice, in agreement with the magnetic structure determination.[17] The energy dependence of the magnetic intensity through the *K* edge, between 6.52 and 6.58 keV, was observed without polarization analysis at $T=20$ K. Figure 1 summarizes the results obtained at the $(\frac{1}{2},-\frac{1}{2},\frac{5}{2})$ reflection. The top part shows the fluorescence as determined by fitting the incoherent background below the magnetic peak; the center part shows the variation of the integrated intensity with the incident photon energy, while the bottom part illustrates the evolution of the rocking curve width. The broadening observed near the absorption edge [Fig. 1(c)] is due to the change in the penetration depth. The magnetic intensity [Fig. 1(b)] exhibits striking features at energies corresponding exactly to the different maxima in the fluorescence at 6.545, 6.549, and 6.551 keV [Fig. 1(a)]. The resonant effects can be summarized as follows: (i) there exist large enhancements of scattered intensities at photon energies at the $4p$ threshold above the *K* edge over an energy range of 10 eV; and (ii) a dip and an oscillatory behavior are observed near the $3d$ threshold where virtual transitions to the strongly spin-polarized $3d$ states are expected; this energy corresponds to the prepeak seen in the fluorescence data. Very similar features have been observed on three other magnetic reflections $(\frac{1}{2},-\frac{1}{2},\frac{3}{2})$, $(\frac{1}{2},-\frac{1}{2},\frac{7}{2})$, and $(\frac{1}{2},\frac{1}{2},\frac{5}{2})$. A quantitative interpretation requires that the data be corrected for absorption. The results are shown in Fig. 2 for all four mea-

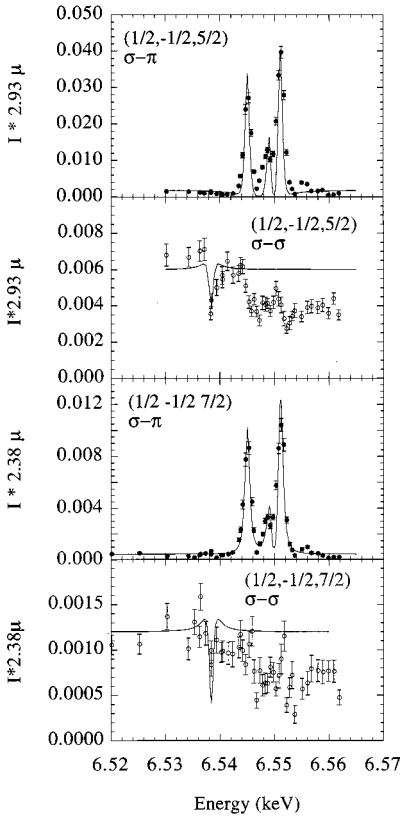

FIG. 3. Polarization analysis at the $(\frac{1}{2},-\frac{1}{2},\frac{5}{2})$ and $(\frac{1}{2},-\frac{1}{2},\frac{7}{2})$ reflections as a function of photon energy. Each data point corresponds to intensity integrated over the sample angle. The lines in the σ-π channel are the results of the calculations described in Secs. V A and V B; each of the three $E1$ resonances contributes with the same adjustable parameter $(\Delta/\Gamma_c)\delta$ for the two reflections (see text in Sec. V A). The lines in the σ-σ channel show the $E2$ contribution (see text in Sec. V B).

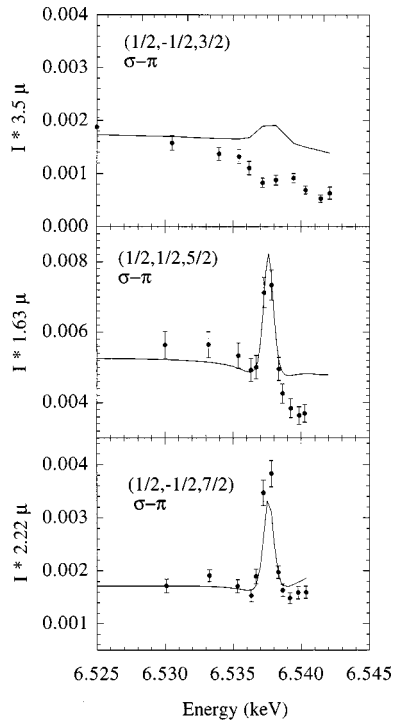

FIG. 4. Energy dependence of the intensities of the $(\frac{1}{2},-\frac{1}{2},\frac{3}{2})$, $(\frac{1}{2},\frac{1}{2},\frac{5}{2})$, and $(\frac{1}{2},-\frac{1}{2},\frac{7}{2})$ reflections in the rotated channel σ-π at the quadrupolar threshold. The lines are the results of calculations in the simple spin-orbit splitting model described in Sec. V B including the dipolar contributions. The same adjustable parameters (apart from the scale factor) were used for all reflections in the σ-π and the σ-σ channels. The coefficients for the absorption corrections are slightly different from those in Fig. 3, because the two measurements have been performed with a different sample orientation. It is seen that absorption corrections above the K edge are underestimated.

sured reflections together with the fluorescence signal. It is noteworthy that even if the corrected intensities on both sides of the absorption edge are similar, the high-energy intensities are consistently lower, indicating that the absorption corrections are underestimated. The energy line shape for all the measured reflections is very similar, the only difference being the variation of resonant intensities with Bragg peak position (h,k,l). It should be noted that the maxima in the $E1$ resonant intensity coincide with peaks in the fluorescence spectrum, even before absorption corrections are made. Resonant enhancements by a factor of 10 are observed, which is as strong as that observed in light rare earths.[25]

In order to identify the origin of the resonances, two experiments were conducted to perform polarization analysis at the $(\frac{1}{2},-\frac{1}{2},\frac{5}{2})$ and $(\frac{1}{2},-\frac{1}{2},\frac{7}{2})$ reflections that show the largest measured resonant intensity. The $4p$ threshold was studied in the first experiment; the results are displayed in Fig. 3 where all intensities are given on the same arbitrary scale. Only the rotated polarization channel (σ-π) exhibits resonant effects with a line shape similar to the ones shown in Fig. 2. This indicates that the strong resonances observed in $RbMnF_3$ arise from $E1$ transitions to the $4p$ states.[1,2]

In the second experiment, we concentrated on the peculiar behavior observed at the prepeak energy (indicated by a vertical arrow in Fig. 1). Note that intensities given in arbitrary units from the same reflections differ from one experiment to the other roughly by a factor of 3 owing to the change of the normalization device. The results are shown in Figs. 4 and 5 for the three studied reflections $(\frac{1}{2},-\frac{1}{2},\frac{3}{2})$, $(\frac{1}{2},\frac{1}{2},\frac{5}{2})$, and $(\frac{1}{2},-\frac{1}{2},\frac{7}{2})$. The two reflections $(\frac{1}{2},\frac{1}{2},\frac{5}{2})$ and $(\frac{1}{2},-\frac{1}{2},\frac{7}{2})$ show an interesting resonant behavior: in the rotated channel σ-π, the scattered intensity increases by about 50% at the $3d$ threshold, whereas the nonrotated channel σ-σ exhibits a dip of similar magnitude at the same photon energy. These effects are barely noticeable at the $(\frac{1}{2},-\frac{1}{2},\frac{3}{2})$ where strong interference effects between the nonresonant scattering amplitude and the dipole resonance are clearly visible.

Finally, we have studied the temperature dependence of magnetic intensities at the $(\frac{1}{2},\frac{1}{2},\frac{5}{2})$ reflection in σ-π both in the nonresonant regime and at the maximum of the resonance (6.5 keV and 6.551 keV, respectively). The results are shown in Fig. 6, where they are compared with the temperature dependence of the $(\frac{1}{2},\frac{1}{2},\frac{1}{2})$ reflection measured using neutron diffraction from the same crystal on the four-circle diffractometer D10 at the Institut Laue Langevin. Neutron intensities have been corrected for extinction. Even if the ordering temperatures deduced from all measurements are identical ($T_N = 84$ K), the temperature dependence of the x-ray intensities is actually different from the neutron observations. However, the neutron-diffraction experiments have

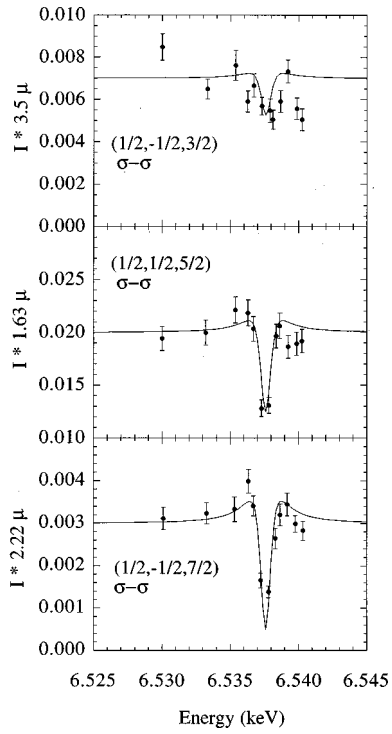

FIG. 5. Energy dependence of the intensities of the $(\frac{1}{2},-\frac{1}{2},\frac{3}{2})$, $(\frac{1}{2},\frac{1}{2},\frac{5}{2})$, and $(\frac{1}{2},-\frac{1}{2},\frac{7}{2})$ reflections in the nonrotated channel σ-σ at the quadrupolar threshold. The lines are the results of calculations in the simple spin-orbit splitting model described in Sec. V B including the dipolar contributions. The same adjustable parameters (apart from the scale factor) were used for all reflections in the σ-π and the σ-σ channels. See caption of Fig. 4 for the coefficients for absorption corrections.

revealed the multigrain structure of the sample and the agreement is reasonable considering the experimental uncertainties: a possible explanation would be that neutrons and 6.5-keV x rays do not probe the same sample (neutrons see the bulk of the sample whereas soft x rays are limited to a near-surface region).

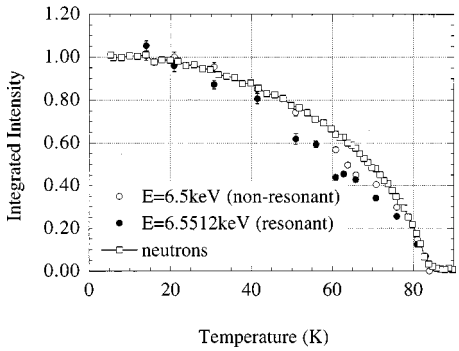

FIG. 6. Temperature dependence of the $(\frac{1}{2},-\frac{1}{2},\frac{5}{2})$ reflection measured in the σ-π channel at 6.551 keV in the resonant regime (full circles) and at 6.50 keV in the nonresonant regime (open circles), compared with the temperature dependence of the $(\frac{1}{2},\frac{1}{2},\frac{1}{2})$ reflection measured with neutron scattering corrected for extinction.

IV. MAGNETIC SCATTERING AMPLITUDES

In the following, we will address the question of the possible mechanisms for the magnetic resonance by comparing our experimental results with predictions from existing models. Our data extend over a wide range of photon energy, which allows comparison between nonresonant and resonant intensities: the normalization of resonant scattering intensities to the nonresonant intensities provides a measure of the resonant scattering amplitude. We will now successively discuss the two regimes.

A. Nonresonant magnetic scattering

Magnetic x-ray scattering arises from the interaction between the electromagnetic field and the electronic spin and current operators.[26,27] When the photon energy is far from photoabsorption resonances, the nonresonant (NRXS) magnetic scattering amplitude $f_{\mathrm{nonres}}(Q)$ per Mn site can be written as[28]

$$f_{\mathrm{nonres}}(Q)=\begin{bmatrix} f_{\sigma\to\sigma} & f_{\pi\to\sigma} \\ f_{\sigma\to\pi} & f_{\pi\to\pi} \end{bmatrix} = -ir_0\frac{\hbar\omega}{mc^2}2\sin\theta\begin{bmatrix} \cos\theta\, S_2(Q) & -\sin\theta\{\cos\theta[L_1(Q)+S_1(Q)]-\sin\theta\, S_3(Q)\} \\ \sin\theta\{\cos\theta[L_1(Q)+S_1(Q)]+\sin\theta\, S_3(Q)\} & \cos\theta[2\sin^2\theta\, L_2(Q)+S_2(Q)] \end{bmatrix}, \tag{1}$$

where $Q=k_i-k_f$ is the scattering vector with incident and scattered wave vectors k_i and k_f; θ denotes the Bragg angle. The vectors $\mathbf{S}(Q)$ and $\mathbf{L}(Q)$ contain the spin and orbital magnetic form factors, respectively. They are given by their components in a standard coordinate system u_1,u_2,u_3,[28] where u_1 is directed along k_i+k_f, u_2 is perpendicular to the scattering plane and parallel to $k_i\times k_f$, and u_3 is along Q. A matrix form for the scattering amplitude is used to represent the polarization dependence; the basis vectors for the polarization ε_i and ε_f correspond to a linear polarization either perpendicular (σ) or parallel (π) to the scattering plane.

In the case of $L=0$ such as Mn^{2+}, $f_{\mathrm{nonres}}(Q)$ reduces to

$$f_{\mathrm{nonres}}(Q)=-ir_0\frac{\hbar\omega}{mc^2}2Sf_m(Q)\sin\theta\begin{bmatrix} \cos\theta\, z_2 & -\sin\theta[\cos\theta z_1-\sin\theta z_3] \\ \sin\theta[\cos\theta\, z_1+\sin\theta\, z_3] & \cos\theta\, z_2 \end{bmatrix}, \tag{2}$$

where $2S\mu_B$ is the ordered magnetic moment per site and $f_m(Q)$ is the spin-only magnetic form factor. $\mathbf{z}$ is a unit vector along the magnetization direction. The nonresonant scattering amplitude can be explicitly calculated when the amplitude and

direction of the magnetic moments are known. In the case of $RbMnF_3$, we obtain $|f_{\rm nonres}|=2S(\hbar\omega/mc^2)r_0\approx 5.5\times10^{-2}r_0$ at the K edge as a prefactor for the geometrical dependence in Eq. (2).

B. Resonant regime

Taking into account the presence of absorption edges, the magnetic resonant scattering amplitude can be expressed as[27]

$$f_n^{\rm res}(k_i,k_f,\varepsilon_i,\varepsilon_f,\hbar\omega)=-\frac{r_0}{m}\sum_{a,cj}\sum p_a p_a(c) \times\frac{E_a-E_c}{\hbar\omega}\frac{\langle a|[\varepsilon_f\cdot P_j-i\hbar(k_f\times\varepsilon_f)\cdot s_j]e^{-ik_f\cdot r_j}|c\rangle\langle c|[\varepsilon_i\cdot P_j+i\hbar(k_i\times\varepsilon_i)\cdot s_j]e^{ik_i\cdot r_j}|a\rangle}{E_a-E_c+\hbar\omega-i\Gamma_c/2}. \quad (3)$$

Here s_j denotes the electronic spin operator. The summation is over all possible initial states $|a\rangle$ of energy E_a and probability p_a, and intermediate levels $|c\rangle$ of energy E_c where one electron is excited to the intermediate state leaving a hole in the core level of the initial state. $p_a(c)$ gives the probability that the intermediate state is unoccupied in $|a\rangle$. Γ_c represents the lifetime of the core hole; in the following we will use the reduced energy scale $x=2(\hbar\omega-E_c+E_a)/\Gamma_c$.

Before discussing the various resonant process, we must consider the appropriate energy scales which govern the electronic structure of $3d$ systems where both the $3d$ and the $4p$ states can contribute to resonant scattering. In $RbMnF_3$, the Mn^{2+} ions are in the $3d^5$ configuration with an ^6S ground state according to Hund's rules. In the presence of a large cubic crystalline field, Hund's rules may break down and the ground state would become an orbital (low-spin) triplet (symmetry $^2T_{2g}$). Estimates for the crystal-field parameter ($\approx$0.15 eV) are comparable to the Racah parameter that characterizes the free-atom energies ($\approx$0.1 eV) in Mn^{2+} ions[29,30] and we can assume that the Mn^{2+} are in the ^6S state. This is corroborated by the weak magnetic anisotropy in the ordered state as measured by antiferromagnetic resonance.[21] In $RbMnF_3$, the $3d$ states form a very narrow band which consists of filled $3d\downarrow$ subbands and one unoccupied $3d\uparrow$ subband. Despite the $L=0$ ground state value, spin-orbit coupling is present in the $3d$ states with characteristic splitting values $\Delta_{3d}\approx 0.04$ eV.[31]

In contrast with the $3d$ levels, the $4p$ states form an extended band (10 eV wide) above the $3d$ levels with a weak spin-orbit splitting $\Delta_{4p}\approx 0.01$ eV and, possibly a small spin polarization, m_{4p}. Owing to the O_h point symmetry of the Mn^{2+} sites, there is no mixing of the $3d$ and $4p$ states; $E1$ transitions connect the $1s$ core level to the $4p$ levels only while $E2$ transitions lead to pure $3d$ states. The observation that the $E1$ resonance extends over 10 eV indicates that probably the whole $4p$ band contributes to the resonance. Nevertheless, in this paper, we will restrict ourselves to an atomic picture and we will consider transitions from the $1s$ core level to ideally narrow $3d$ and $4p$ states at resonant energies E_K^{3d} and E_K^{4p}; they correspond to the prepeak and white line energies in the fluorescence spectrum in Fig. 2 at 6.538 keV and around 6.550 keV, respectively. We note that in $RbMnF_3$ the $4p$ bands are empty with no net $4p$ magnetization; nevertheless, we will consider the general case of partially occupied $4p$ bands with n_h holes ($0\leqslant n_h\leqslant 6$) and a partial spin polarization m_{4p} ($0\leqslant m_{4p}\leqslant 3$).

Three contributions to the resonant scattering amplitude in Eq. (3) should be considered:[24,29] a pure spin-spin term, $(k_f\times\varepsilon_f\cdot s)(k_i\times\varepsilon_i\cdot s)$, a cross term involving the electron spin operator, $(\varepsilon_f\cdot P)(k_i\times\varepsilon_i\cdot s)-(k_f\times\varepsilon_f\cdot s)(\varepsilon_i\cdot P)$, and finally a purely orbital term, $(\varepsilon_f\cdot P)(\varepsilon_i\cdot P)$. The pure spin-spin resonant term, $(k_f\times\varepsilon_f\cdot s)(k_i\times\varepsilon_i\cdot s)$ does not give rise to antiferromagnetic Bragg peaks, although it contributes to the anomalous scattering.[27]

The cross term $(\varepsilon_f\cdot P)(k_i\times\varepsilon_i\cdot s)-(k_f\times\varepsilon_f\cdot s)(\varepsilon_i\cdot P)$ was considered by Namikawa *et al.* in the case of Ni metal.[1] This model involves electric and magnetic transitions to the $4p$ states only. Neglecting spin-orbit coupling in the $4p$ levels, we have rederived the following expression for the resonant amplitude:[1,32]

$$f_{\rm Nam}=-ir_0\frac{(ka_0)^2}{12}\left|\left\langle 1s\left|\frac{r}{a_0}\right|4p\right\rangle\right|^2\frac{E_K^{4p}}{\Gamma_c}\frac{m_{4p}}{x_{4p}-i} \times\sin 2\theta\begin{bmatrix}0 & -\sin\theta z_1+\cos\theta z_3\\ \sin\theta_1+\cos\theta z_3 & 2z_2\end{bmatrix}, \quad (4)$$

where m_{4p} is the spin polarization of the $4p$ holes and a_0 the Bohr radius. $\langle 1s|r/a_0|4p\rangle$ is the $E1$ radial matrix element. This expression for $f_{\rm Nam}$ in Eq. (4) is equivalent to the result previously derived.[1] From Eq. (4), we note that this resonant process predicts the absence of resonant intensity in the σ-σ polarization channel, similarly to Hannon's model;[2] more importantly, it does not induce a magnetic circular dichroism signal because $f_{\rm Nam}$ vanishes at $Q=0$. Therefore, this mechanism cannot account for magnetic resonances leading to a magnetic x-ray dichroism signal.[13–15]

The last contribution to the resonance arises from the purely orbital term $(\varepsilon_f\cdot P)(\varepsilon_i\cdot P)$ in Eq. (3). As pointed out by Hannon *et al.*,[2] these multipolar electric transitions couple to the magnetization if there exists spin-orbit coupling in either the core level or the excited states. The magnetic sensitivity arises from the spin polarization and the exchange splitting in the intermediate states. At the K edge, neglecting exchange splitting in the $1s$ level, the absence of spin-orbit interaction in the core level implies that some asymmetry exists in the excited states. Spin-orbit coupling in the $4p$ states was previously introduced to account for the circular dichroism observed in Fe.[13] Let us first discuss the $E1$ tran-

sitions. The asymmetry between $4p\uparrow$ and $4p\downarrow$ states arises from m_{4p}, the net number of polarized $4p$ electrons, and from the exchange splitting J induced by the $3d$ moments between the up- (lower energy) and the down-spin states (upper energy). We have also included the possibility for breathing effects due to the difference between radial transition matrix elements:[33]

$$\left\langle 1s\left|\frac{r}{a_0}\right|4p,\ \ \sigma=\uparrow\ \text{ or }\ \downarrow\right\rangle=\left\langle 1s\left|\frac{r}{a_0}\right|4p\right\rangle_{\mathrm{Av}}(1\pm\delta/2) \quad (5)$$

The transition probabilities[2] are summed over the $j=\frac{1}{2}$ and $j=\frac{3}{2}$ multiplets separated by the spin-orbit splitting Δ_{4p}, small compared to $\Gamma_c/2$. Following the method of Ref. 2, we obtain the $E1$ part of the resonant scattering amplitude as

$$\begin{aligned} f_{E1}=&ir_0\frac{4}{27}(ka_0)^2\left|\left\langle 1s\left|\frac{r}{a_0}\right|4p\right\rangle\right|^2\\ &\times\frac{E_K^{4p}}{\hbar\omega}\frac{mc^2}{\Gamma_c}\frac{1}{(x_{4p}-i)^2}\frac{\Delta_{4p}}{\Gamma_c}\\ &\times\left[(m_{4p}-n_h\delta)+2n_h\frac{J}{\Gamma_c}\frac{1}{(x_{4p}-i)}\right]\\ &\times\begin{bmatrix}0 & \cos\theta z_1+\sin\theta z_3\\ -\cos\theta z_1+\sin\theta z_3 & -\sin 2\theta z_2\end{bmatrix}, \end{aligned} \quad (6)$$

where n_h is the total number of holes available in the $4p$ band and m_{4p} is the net number of spin-up $4p$ electrons. The energy profile is not a simple Lorentzian shape because the two energy scales, Δ and J, induce small energy shifts in the usual Lorentzian, leading to first- and second-derivative profiles. In principle, the analysis of the energy line shape would make it possible to disentangle the spin-orbit and the exchange splittings.

Now we consider the $E2$ scattering amplitude. In the Mn^{2+} ground state, the ^6S term of the $(1s^2,3d^5)$ configuration, the probabilities for transitions from $1s$ to the $3d$ available states summed over the $j=\frac{3}{2}$ and $j=\frac{5}{2}$ multiplets are equal because all spin-up (down) states are unoccupied (occupied) in Mn^{2+}. If we neglect the spin-orbit splitting Δ_{3d} between the $j=\frac{3}{2}$ and $j=\frac{5}{2}$ states in the intermediate state $(1s^1,3d^6)$, there is no magnetic resonance with the classical resonating denominator $1/(x_{3d}-i)$, in agreement with Ref. 4 for the $L=0$ case. Nevertheless, if we take into account this energy splitting, there appears a weak contribution with $1/(x_{3d}-i)^2$ as energy profile, which is the first derivative of the usual resonant term, similarly to the $E1$ case. Within this crude model, there exist simple symmetry relations between transition amplitudes from the core level $|1s\rangle$ to the different $|l=2,m_l\rangle$ states which make the $E2$ scattering amplitude linear in the magnetization unit vector of the $3d$ electrons, z, although in the general case it contains terms up to the 4th order in z.[2,25] Restricting ourselves to the magnetic part of the resonant scattering amplitude, we find that

$$\begin{aligned} f_{E2}=&-ir_0\frac{1}{75}(ka_0)^4\left|\left\langle 1s\left|\left(\frac{r}{a_0}\right)^2\right|3d\right\rangle\right|^2\frac{E_K^{3d}}{\hbar\omega}\frac{mc^2}{\Gamma_c}\frac{\Delta_{3d}}{\Gamma_c}\frac{1}{(x_{3d}-i)^2}\\ &\times\begin{bmatrix}\sin 2\theta z_2 & \cos\theta(1-2\cos 2\theta)z_1-\sin\theta(1+2\cos 2\theta)z_3\\ -\cos\theta(1-2\cos 2\theta)z_1-\sin\theta(1+2\cos 2\theta)z_3 & 4\sin 2\theta\cos 2\theta z_2\end{bmatrix}. \end{aligned} \quad (7)$$

It should be noted that this model predicts resonant effects in the rotated and unrotated polarization channels, in agreement with the experimental observations.

The models that have been used above are certainly oversimplified and cannot provide an accurate amplitude. In particular, all the intermediate states have been treated as atomiclike. Nevertheless, it is instructive to extract some orders of magnitude for the predicted resonant amplitudes. At this point, it is worth noting that $|f_{\mathrm{Nam}}|$ is reduced by $\hbar\omega/mc^2$ compared to $|f_{E1}|$; this is in agreement with usual comparisons between magnetic and electric transitions. In the ionic compound $RbMnF_3$, there is no electron in the $4p$ band, $n_h=6$ and $m_{4p}=0$; therefore, f_{Nam} vanishes, Eq. (4). This means that, within the approximations leading to Eq. (4), the $(\varepsilon_f\cdot P)(k_i\times\varepsilon_i\cdot s)$ term in the scattering amplitude cannot represent the observed resonance in $RbMnF_3$ at the K edge. Now let us consider the $(\varepsilon_f\cdot P)(\varepsilon_i\cdot P)$ contribution, Eqs. (6) and (7). The $E1$ and $E2$ radial matrix elements can be taken as 2.5×10^{-3} and 7×10^{-4}, respectively,[34] and the spin-orbit splitting of $3d$ states $\Delta_{3d}\approx0.04$ eV.[31] The value $\Gamma_c=1.1$ eV for the core-hole lifetime was extracted from the fluorescence data,[35] and is in agreement with calculated values.[36] At the Mn K edge, $(ka_0)^2\approx3$. Educated guesses for the other parameters ($\Delta_{4p}\approx0.05$ eV, $\delta\approx0.01$ and/or $J\approx5$ meV) lead to $|f_{E1}|\approx4\times10^{-3}r_0$ and $|f_{E2}|\approx1\times10^{-3}r_0$ at the resonant energy. These estimates for the $E1$ and $E2$ resonant scattering amplitudes yield values that are smaller than the nonresonant scattering amplitude $|f_{\mathrm{nonres}}|$ at $Q=0$. In the following, we will compare the observed resonant with the nonresonant scattered intensities. The nonmagnetic part of the total x-ray scattering amplitude can be assessed by a correlation with the fluorescence. The fluorescence curve [Fig. 1(b)] has been transformed into the imaginary part f'' of the scattering amplitude; at the $E1$ the white line is experimentally found to contribute up to 16 electrons, whereas the $E2$ contribution is around 0.09 electrons. Our model gives 12 and 0.07 electrons at the $E1$ and $E2$ threshold, respectively, indicating that the resonant scattering amplitudes are realistic. It should be stressed that the energy line shape of the fluorescence in Fig. 2 shows that the $4p$ states must be treated as bands. However, such an approach is beyond the scope of this paper.

The total scattering amplitude is the sum of the resonant and the nonresonant parts given in Eqs. (2), (6), and (7).

TABLE I. Integrated intensities in arbitrary units at 6.50 keV compared to the predicted angular dependence in the case of uniformly distributed magnetic *T* domains. Scaling the angular factor by 0.61 shows an excellent agreement between the experimental results and the predicted *Q* dependence.

(*h*,*k*,*l*)	Intensities	$\tan\theta f_m^2(Q)$
$(\frac{1}{2},-\frac{1}{2},\frac{3}{2})$	0.11±0.01	0.18
$(\frac{1}{2},-\frac{1}{2},\frac{5}{2})$, $(\frac{1}{2},\frac{1}{2},\frac{5}{2})$	0.07±0.02	0.13
$(\frac{1}{2},-\frac{1}{2},\frac{7}{2})$	0.019±0.002	0.03

Usually, the magnetic structure factors are then calculated and transformed in scattering cross sections by using a density-matrix formalism to account for the polarization of the radiation.[28] Here, in order to simplify the analysis, we will assume a perfectly linearly polarized incident beam.

V. COMPARISONS AND DISCUSSIONS

As mentioned above, there exist four magnetic domains in $RbMnF_3$ which all contribute to a given Bragg peak at *Q*, and magnetic intensities must be averaged over the magnetic domain populations. A full determination of the domain fraction would require measurements of the azimuthal dependence of polarized intensities. Here, we assume that all domains are evenly populated and we make use of the relation $\langle z_u z_v\rangle=\frac{1}{3}\delta_{uv}$, valid in cubic symmetry, when calculating scattered intensities. This hypothesis can be verified by considering the observed nonresonant intensities. By including the appropriate Lorentz factor $L=\sin 2\theta$,[37] we obtain from Eq. (2)

$$I^{\sigma\sigma}=\frac{N}{3}r_0^2\frac{(\sin\theta)^2}{\sin 2\theta}(\cos\theta)^2A_{\text{nonres}}^2f_m^2(Q),$$

$$I^{\sigma\pi}=\frac{N}{3}r_0^2\frac{(\sin\theta)^4}{\sin 2\theta}A_{\text{nonres}}^2f_m^2(Q), \tag{8}$$

where *N* is a scale factor and $A_{\text{nonres}}=(\hbar\omega/mc^2)2S$. The spin-only magnetic form factor can be taken from Ref. 38. When no polarization analysis is performed, the scattered intensity from a linearly polarized beam reduces to

$$I=\frac{N}{3}r_0^2\frac{\tan\theta}{2}A_{\text{nonres}}^2f_m^2(Q). \tag{9}$$

In Table I, measurements of total intensities at 6.5 keV are compared with the predicted angular dependence in Eq. (9). The observed relative agreement with the predicted values supports our assumption about the domain distribution.

We will now discuss the energy dependence of magnetic intensities across the $E1$ (E_K^{4p}) and the $E2$ (E_K^{3d}) resonances. For the sake of simplicity, we ignore the variation of quantities such as $\hbar\omega/mc^2$, $E_K^{3d}/\hbar\omega$, and $E_K^{4p}/\hbar\omega$ in Eqs. (2)–(7) over the energy range that we have studied. We have used broadened energy line shapes (effective $\Gamma_c\approx 1.5$ eV) in order to take into account the finite energy resolution of the spectrometer.

A. Dipolar threshold

Leaving aside the $(k_f\times\varepsilon_i\cdot s)(\varepsilon_i\cdot P)$ term, we concentrate on the $(\varepsilon_f\cdot P)(\varepsilon_i\cdot P)$ model which leads to

$$I_{E1}^{\sigma\pi}=\frac{N}{3}r_0^2\frac{1}{\sin 2\theta}\left[\sin^4\theta\, f_m^2(Q)A_{\text{nonres}}^2+A_{E1}^2\left(\frac{1}{1+x_{4p}^2}\right)^2-2\sin^2\theta\cos 2\theta\, f_m(Q)A_{\text{nonres}}A_{E1}\frac{1-x_{4p}^2}{(1+x_{4p}^2)^2}\right], \tag{10}$$

where

$$A_{E1}=\frac{4}{27}(ka_0)^2\left|\left\langle 1s\left|\frac{r}{a_0}\right|4p\right\rangle\right|^2\frac{E_K^{4p}}{\hbar\omega}\frac{mc^2}{\Gamma_c}\frac{\Delta_{4p}}{\Gamma_c}n_h\delta_{\text{eff}}.$$

In the absence of $4p$ electrons ($n_h=6$ and $m_{4p}=0$) the breathing δ and the exchange splitting J/Γ_c play a similar role [see Eq. (6)]. As mentioned below, the broad energy line shape of the $E1$ resonance prevents any comparison between (Lorentzian)^2 and (Lorentzian)^3 profiles which would help in distinguishing the two contributions. For the sake of simplicity we have assumed a (Lorentzian)^2 profile with an effective adjustable parameter $(\Delta_{4p}/\Gamma_c)\delta_{\text{eff}}$.

As shown from Figs. 2 and 3, the resonance at the $4p$ threshold forms a wide band in energy significantly broader than the core-hole lifetime, Γ_c, with peaks corresponding to maxima of the energy-dependent absorption coefficient. Similar broad resonances in the vicinity of the $4p$ threshold have been observed in several other RXMS experiments[8,9] and magnetic circular dichroism studies.[13–15] Their origin arises from the presence of the broad $4p$ bands or alternatively from multiple-scattering processes. The variation of the resonant amplitude with the photon energy reflects the variation of the density of spin-polarized states across the $4p$ band. Spikes similar to those observed in Figs. 2 and 3 have also been found in band calculations for Mn oxides.[39] It is beyond the scope of this paper to represent the band nature of the resonance. In the simplest model, the dipole-projected density of states which gives the white line and the fluorescence yield is expected to be responsible for the magnetic resonant scattering. In this manner we have minimized the number of parameters by choosing three resonances centered at 6.545, 6.549, and 6.551 keV, i.e., at the peaks in the fluorescence signal.

The modeling of the data in the σ-π channel at the $(\frac{1}{2},-\frac{1}{2},\frac{5}{2})$ and the $(\frac{1}{2},-\frac{1}{2},\frac{7}{2})$ positions by the $(\varepsilon_f\cdot P)(\varepsilon_i\cdot P)$ scattering amplitude Eq. (10) is shown in Fig. 3. For the two reflections, each resonance contributes to $2-3\times10^{-2}r_0$. The full lines in Fig. 3 have been calculated with $(\Delta_{4p}/\Gamma_c)\delta_{\text{eff}}$ equal to 3.5×10^{-3}, 2.5×10^{-3}, and 4.0×10^{-3} for the three resonances, respectively. Taking $\delta_{\text{eff}}\approx 0.05$ ($\delta\approx 0.05$ or $J\approx 0.02$ eV) leads to an average value $\Delta_{4p}\approx 0.07\pm 0.01$ eV. These values are consistent with accepted values for exchange breathing and spin-orbit splitting in the $4p$ states.[34] No information is available on the size of the exchange splitting of the $4p$ bands induced by the antiferromagnetic ordering of the $3d$ moments. Core-level photoemission studies on Fe metal have provided values of the exchange splitting of the $2p$ states in the 0.3–0.5 eV.[40] Simi-

lar values for J would lead to a much stronger $E2$ resonance than observed in $RbMnF_3$. Furthermore, the calculated Q dependence is in qualitative agreement with the data. The values obtained above may not represent the sole best fit but they are physically acceptable and we can conclude that the $(\varepsilon_f \cdot P)(\varepsilon_i \cdot P)$ term in the resonant scattering process can explain the amplitude of the dipole resonance at the K edge. Obviously, the energy profile of the resonance is not well reproduced but it can only be explained if the electronic band structure of $RbMnF_3$ is taken into account.

B. Quadrupolar threshold

Now let us turn to the narrow quadrupole resonance which is observed in the two polarization channels. In the vicinity of the $3d$ threshold, we consider the interference between the nonresonant scattering amplitude and f_{E2}. The energy dependence of the polarized intensities reads as

$$I^{\sigma\sigma}=\frac{N}{3}r_0^2\frac{(\sin 2\theta)^2}{\sin 2\theta}\left[\frac{f_m^2(Q)}{4}A_{\text{nonres}}^2 - f_m(Q)A_{\text{nonres}}A_{E2}\frac{1-x_{3d}^2}{(1+x_{3d}^2)^2}+A_{E2}^2\frac{1}{(1+x_{3d}^2)^2}\right],$$

$$I^{\sigma\pi}=\frac{N}{3}r_0^2\frac{1}{\sin 2\theta}\left[\sin^4\theta\, f_m^2(Q)A_{\text{nonres}}^2+A_{E2}^2\frac{1}{(1+x_{3d}^2)^2} - 2\sin^2\theta(2\cos^2 2\theta-1)f_m(Q)A_{\text{nonres}}A_{E2}\frac{1-x_{3d}^2}{(1+x_{3d}^2)^2}\right], \tag{11}$$

where

$$A_{E2}=\frac{1}{75}(ka_0)^4\left|\left\langle 1s\left|\left(\frac{r}{a_0}\right)^2\right|3d\right\rangle\right|^2\frac{E_K^{3d}}{\hbar\omega}\frac{mc^2}{\Gamma_c}\frac{\Delta_{3d}}{\Gamma_c}$$

is the $E2$ resonant amplitude with Δ_{3d} as the only adjustable parameter. The full lines in Figs. 4 and 5 represent the energy profiles given by Eq. (11) with $\Delta_{3d}\approx 0.08\pm 0.01$ eV adjusted to fit the data with an $E2$ resonant amplitude of $2\times 10^{-3}r_0$. The presence of the dipole resonances was taken into account with the $E1$ parameters given above; calculations are given in Fig. 3. In the σ-π channel, the interference between nonresonant and resonant $E1$ scattering is not well reproduced; this is because the energy profile of the $E1$ part cannot be explained without band calculation. Nevertheless, the $E2$ resonant behavior for the three measured reflections are qualitatively well represented by the predictions based on the $E2$ transitions due to the $(\varepsilon_f \cdot P)(\varepsilon_i \cdot P)$ operator with only one parameter. The value obtained for Δ_{3d} is appropriate for $3d$ states even if it is slightly larger than anticipated;[31] this confirms the validity of the proposed model based on electric multipole transitions.[2]

VI. CONCLUSIONS

The observation of the magnetic resonant process in $RbMnF_3$ has revealed the existence of two different resonant regimes. Near the $4p$ threshold, large resonant enhancements of the magnetic intensities can be seen over a wide range of photon energy corresponding to the width of the Mn $4p$ band. The $3d$ threshold shows only weak oscillations in the scattered intensities over a narrow energy range governed by the core-hole lifetime. By studying carefully the energy dependence of the polarized scattered intensities from $RbMnF_3$ at different Q values, we have been able to show that the mechanism of multipole electric transitions accounts qualitatively well for the observed resonant amplitudes at the Mn K edge. In particular, the existence of spin-orbit splitting ($\Delta_{3d}\approx 0.08$ eV) in the $3d$ states explains quantitatively the quadrupolar resonance, even in the absence of net orbital moment in the ground state of the $3d^5$ configuration. The amplitude of the dipolar resonance is found to arise from the spin-orbit splitting ($\Delta_{4p}\approx 0.07$ eV) in the $4p$ band together with weak exchange splitting; this exchange splitting manifests itself as an energy splitting of the empty Mn $4p$ band together with a small breathing effect in the radial matrix elements which we cannot differentiate. The obtained values appear to be realistic, even if the modeling of the observed magnetic x-ray scattering intensities leads to approximate results only. However, there remain several open questions. A significant feature in our experimental results is the existence of broadbands of resonance extending over 10 eV which correspond to the width of the $4p$ bands. A deeper understanding of this phenomenon requires resorting to calculations of the electronic density of states either at the cluster level or at a more extended scale; band calculations could indicate whether the magnetic sensitivity of the resonance extends across the whole $4p$ band. Another open question has to do with the strength of the dipole resonance. In several antiferromagnetic insulating $3d$ compounds that have been studied,[8,9] the observed resonant enhancements are found to be rather large (a factor of about 3 at the quadrupole energy and around 10 at the dipole threshold), whereas in ferromagnetic Ni metal,[1] this effect appears to be much weaker. Again a model for the resonance based on a band picture would be highly desirable. It is hoped that the experimental results presented in this paper will stimulate the necessary further theoretical work.

ACKNOWLEDGMENTS

Illuminating discussions with M. Altarelli and P. Carra are sincerely acknowledged. We thank N. Manini and P. Carra for their calculations of radial matrix elements.

*Present address: XMAS CRG at ESRF, BP 220, F-38043 Grenoble Cedex, France.

†Present address: MUCAT, Argonne National Laboratory, Argonne, IL 60439.

‡Present address: Center d'Etudes Nucléaires, DRFMC/SPSMS/LCP, F-38054 Grenoble Cedex 9, France.

[1] K. Namikawa, M. Ando, T. Nakajima, and H. Kawata, J. Phys. Soc. Jpn. **54**, 4099 (1985).

[2] J. P. Hannon, G. T. Trammell, M. Blume, and D. Gibbs, Phys. Rev. Lett. **61**, 1245 (1988).

[3] D. Gibbs, D. R. Harshmann, E. D. Isaacs, D. B. McWhan, D. Mills, and C. Vettier, Phys. Rev. Lett. **61**, 1241 (1988).
[4] S. W. Lovesey, J. Phys.: Condens. Matter **10**, 2505 (1998).
[5] S. W. Lovesey, O. Fritz, and E. Balcar, J. Phys.: Condens. Matter **10**, 501 (1998).
[6] S. Langridge, J. A. Paixàò, N. Bernhoeft, C. Vettier, G. H. Lander, D. Gibbs, S. Aa. Sørensen, A. Stunault, D. Wermeille, and E. Talik, Phys. Rev. Lett. **82**, 2187 (1999).
[7] J. P. Hill, C-C. Kao, and D. F. McMorrow, Phys. Rev. B **55**, R8662 (1997).
[8] L. Paolasini, C. Vettier, F. de Bergevin, F. Yakhou, D. Mannix, A. Stunault, W. Neubeck, M. Altarelli, M. Fabrizio, P. A. Metcalf, and J. M. Honig, Phys. Rev. Lett. **82**, 4719 (1999).
[9] W. Neubeck, C. Vettier, K.-B. Lee, and F. de Bergevin, Phys. Rev. B **60**, R9912 (1999).
[10] K. D. Finkelstein, Q. Shen, and S. Shastri, Phys. Rev. Lett. **69**, 1612 (1992).
[11] D. H. Templeton and L. K. Templeton, Acta Crystallogr., Sect. A: Cryst. Phys., Diffr., Theor. Gen. Crystallogr. **A36**, 237 (1980); V. E. Dmitrienko, Acta Crystallogr., Sect. A: Found. Crystallogr. **A39**, 29 (1983).
[12] A. Kirfel and W. Morgenroth, Acta Crystallogr., Sect. A: Found. Crystallogr. **A49**, 35 (1993).
[13] G. Schütz, W. Wagner, W. Wilhelm, P. Kienle, R. Zeller, R. Frahm, and G. Materlik, Phys. Rev. Lett. **58**, 737 (1987).
[14] H. Maruyama, I. Harada, K. Kobayashi, and H. Yamazaki, Physica B **208-209**, 760 (1995).
[15] H. Sakurai, F. Itoh, H. Maruyama, A. Koizumi, K. Kobayashi, H. Yamazaki, Y. Tamji, and H. Kawata, J. Phys. Soc. Jpn. **62**, 459 (1993).
[16] D. Bloch, D. Hermann-Ronzaud, C. Vettier, W. B. Yelon, and R. Alben, Phys. Rev. Lett. **35**, 963 (1975).
[17] S. J. Pickart, H. A. Alperin, and R. Nathans, J. Phys. (France) **25**, 565 (1964).
[18] D. T. Teaney, M. J. Freiser, and R. W. H. Stevenson, Phys. Rev. Lett. **9**, 212 (1962).
[19] Y. Shapira and N. F. Oliveira, Jr., Phys. Rev. B **18**, 1425 (1978).
[20] M. J. Freiser, P. E. Seiden, and D. T. Teaney, Phys. Rev. Lett. **10**, 293 (1963).
[21] R. Coldea, R. A. Cowley, T. G. Perring, D. F. McMorrow, and B. Roessli, Phys. Rev. B **57**, 5281 (1998).
[22] J. Ferre, J. Phys. C **16**, 3971 (1983).
[23] A. Stunault, C. Vettier, F. de Bergevin, N. Bernhoeft, V. Fernandez, S. Langridge, E. Lidström, J. E. Lorenzo-Diaz, D. Wermeille, L. Chabert, and R. Chagnon, J. Synchrotron Radiat. **5**, 1010 (1998).
[24] F. Vaillant, Acta Crystallogr., Sect. A: Cryst. Phys., Diffr., Theor. Gen. Crystallogr. **A33**, 967 (1977).
[25] J. P. Hill and D. F. McMorrow, Acta Crystallogr., Sect. A: Found. Crystallogr. **A52**, 236 (1996).
[26] F. de Bergevin and M. Brunel, Acta Crystallogr., Sect. A: Cryst. Phys., Diffr., Theor. Gen. Crystallogr. **A37**, 314 (1981).
[27] M. Blume, J. Appl. Phys. **57**, 3615 (1985).
[28] M. Blume and D. Gibbs, Phys. Rev. B **37**, 1779 (1988).
[29] S. Sugano, Y. Tanabe, and H. Kanimura, in *Multiplets of Transition-Metals Ions in Crystals* (Academic, New York, 1970), p. 112.
[30] Y. Tanabe and S. Sugano, J. Phys. Soc. Jpn. **9**, 766 (1954).
[31] J. S. Griffith, in *The Theory of Transition-Metals Ions* (Cambridge University Press, London, 1961), p. 113.
[32] D. Wermeille, Ph.D. thesis, Ecole Polytechnique de Lausanne, 1988.
[33] M. van Veenendaal, J. B. Goedkoop, and B. T. Thole, Phys. Rev. Lett. **78**, 1162 (1997); M. D. Hamrick, Ph.D. thesis, Rice University, Houston, 1994.
[34] P. Carra and N. Manini (private communications).
[35] F. de Bergevin, M. Brunel, R. M. Galéra, C. Vettier, E. Elkaïm, M. Bessière, and S. Lefèbvre, Phys. Rev. B **46**, 10 772 (1992).
[36] U. Arp, B. M. Lagutin, G. Materlik, I. D. Petrov, B. Sonntag, and V. L. Sukhorukov, J. Phys. B **26**, 4381 (1993).
[37] B. E. Warren, in *X-ray Diffraction* (Dover, New York, 1990), p. 46.
[38] R. Nathans, H. A. Alperin, S. J. Pickart, and P. J. Brown, J. Appl. Phys. **34**, 1182 (1963); R. E. Watson and A. J. Freeman, Acta Crystallogr. **14**, 27 (1961).
[39] I. S. Elfimov, V. I. Anisimov, and G. A. Sawatzky (unpublished).
[40] L. Baumgarten, C. M. Schneider, H. Petersen, F. Schäfers, and J. Kirschner, Phys. Rev. Lett. **65**, 492 (1990).